


NANO EXPRESS

Open Access



Impact of Bi Doping into Boron Nitride Nanosheets on Electronic and Optical Properties Using Theoretical Calculations and Experiments

Muhammad Ikram^{1*} , Muhammad Wakeel², Jahanzeb Hassan², Ali Haider³, Sadia Naz⁴, Anwar Ul-Hamid⁵, Junaid Haider⁴, Salamati Ali², Souraya Goumri-Said⁶ and Mohammed Benali Kanoun^{7*}

Abstract

In the present work, boron nitride (BN) nanosheets were prepared through bulk BN liquid phase exfoliation while various wt. ratios (2.5, 5, 7.5 and 10) of bismuth (Bi) were incorporated as dopant using hydrothermal technique. Our findings exhibit that the optical investigation showed absorption spectra in near UV region. Density functional theory calculations indicate that Bi doping has led to various modifications in the electronic structures of BN nanosheet by inducing new localized gap states around the Fermi level. It was found that bandgap energy decrease with the increase of Bi dopant concentrations. Therefore, in analysis of the calculated absorption spectra, a redshift has been observed in the absorption edges, which is consistent with the experimental observation. Additionally, host and Bi-doped BN nanosheets were assessed for their catalytic and antibacterial potential. Catalytic activity of doped free and doped BN nanosheets was evaluated by assessing their performance in dye reduction/degradation process. Bactericidal activity of Bi-doped BN nanosheets resulted in enhanced efficiency measured at 0–33.8% and 43.4–60% against *S. aureus* and 0–38.8% and 50.5–85.8% against *E. coli*, respectively. Furthermore, In silico molecular docking predictions were in good agreement with in-vitro bactericidal activity. Bi-doped BN nanosheets showed good binding score against DHFR of *E. coli* (−11.971 kcal/mol) and *S. aureus* (−8.526 kcal/mol) while binding score for DNA gyrase from *E. coli* (−6.782 kcal/mol) and *S. aureus* (−7.819 kcal/mol) suggested these selected enzymes as possible target.

Keywords: Boron nitride, Bi-doped boron nitride, Nanosheets, Antimicrobial, HR-TEM

Introduction

Various chemicals, organic compounds, and industrial waste give rise to environmental pollution those results in serious consequences for human, animal, and aquatic life [1, 2]. Due to this reason, innovative and environmentally-friendly wastewater treatment technologies are in growing demand [3, 4]. Millions of people lose their lives each year due to contaminated water [5, 6]. Almost annually dyes utilization is ~10,000 in industrial sectors;

among them, a prominent source is methylene blue (MB) used 10–15% in the atmosphere and aquatic life [7–10]. MB is a simple aniline dye with the molecular formula $C_{16}H_{18}N_3SCl$ that is widely used for dyeing cotton, wool, and silk as well as treating methaemoglobinemia and cyanide poisoning. It is used by biologists to stain tissue samples and to detect nucleic acids. Regardless, this dye has a number of negative effects on both humans and wildlife. As a result, removing dyes from drainage is important for the welfare of humans and aquatic life [11, 12].

Conventional methods used for the elimination of various contaminants from water include precipitation, electrolysis, flocculation, photocatalysis, membrane filtration, ions exchange, adsorption, reverse osmosis and biological treatment [13, 14]. In these methods, catalytic

*Correspondence: dr.muhammadiqram@gcu.edu.pk; mkanoun@kfu.edu.sa

¹ Solar Cell Applications Research Lab, Department of Physics, Government College University Lahore, Lahore 54000, Punjab, Pakistan

⁷ Department of Physics, College of Science, King Faisal University, P.O. Box 400, Al-Ahsa 31982, Saudi Arabia

Full list of author information is available at the end of the article

activity (CA) is widely used due to its cost-effective and environmentally sustainable approach [15]. CA comprises of reducing agent and nanocatalyst which is the prepared sample to degrade synthetic dye such as MB which is the part of present study [16–18].

Increasing requirements to purify wastewater has led to the development and use of a new class of nanomaterials known as two-dimensional materials (2D-Mats). The utilization of these materials was spurred by the discovery of graphene [19–21]. At present, a variety of 2D-Mats has been synthesized including molybdenum disulfide (MoS_2) and MXene (Dirac 2D-Mats) [22, 23]. Boron nitride is considered a promising class of MXene class [24, 25]. BN nanosheets possess several interesting properties including dielectric performance, chemical and thermal stability, deep ultraviolet and direct bandgap energy making it suitable for use in a variety of applications especially for water treatment and antimicrobial activities as well [24, 26, 27]. To state these tasks bismuth-rich strategies or doping with different transition metal elements (i.e. Bi) are the most accessible methodologies. Bi has an extraordinary appearance compared to others showing color-gray-white with a reddish tinge (pinkish stain). Bi forms chemical compounds in oxidation states of +3 and +5. Bi compounds are used as nanocatalyst for wastewater treatment and it is also a good antimicrobial agent when it is utilized as dopant in 2D-Mats such as BN as discussed above [28–31].

In addition to above, BN nanosheets can also be utilized in biomedical sector as a antimicrobial agent with an aim to protect against various bacteria's [32]. Mastitis is distinguished by physicochemical and patho-biological alterations in udder parenchyma tissues, containing direct economic effects worldwide. Humans are at high risk of suffering zoonotic diseases such as leptospirosis, streptococcal sore throat, brucellosis, and tuberculosis due to mastitic milk consumption [33]. Generally, infectious etiological agents that involve bacteria and viruses are categorized into two classes. The first category includes *Staphylococcus aureus* (*S. aureus*), *Coliform*, *Corynebacterium*, *Streptococci* and *Escherichia coli* (*E. coli*). The second category comprises *Corynebacterium bovis* and *coagulase-negative Staphylococci* [2, 32, 34, 35]. Among these, more prominent is *Methicillin-Resistant Staphylococcus aureus* (MRSA) as it contributes to a large number of deaths worldwide. Resistance to antibiotics has emerged in Gram-positive and Gram-negative pathogenic bacteria, posing a serious risk to human health [36]. Besides, diarrheal illness caused by the presence of *E. coli* bacteria in water results in 1.3 million deaths of children below the age of five annually. Being an antibacterial agent, BN protects from these harmful pathogens [37]. Due to Bi's biocompatibility, the synthesis and usage

of Bi in various forms such as Bi salts, NPs, and nanomaterials as antimicrobials has received a huge of attention [38]. Infections caused by *Helicobacter pylori* (*H. pylori*) are currently treated with a mixture of Bi organic salts and antibiotics [39, 40]. The oxidative stress created by nanostructure depends upon its size; concentration and shape as Small-sized nanostructure produce reactive oxygen species (ROS) that bind more efficiently within bacterial membrane within implants resulting in extrusion of cytoplasmic contents and damaging bacterial DNA, proteins, and enzymes [41–43]. Besides ROS production, the strong cationic interface of nanostructures with negatively charged bacteria cell membrane parts results in superior bactericidal activity at high concentrations encouraging bacteria cell collapse [44, 45].

In the present study, BN nanosheets were prepared with chemical exfoliation technique while bismuth (Bi) was incorporated as a dopant using hydrothermal technique. CA of the synthesized material was determined in terms of reduction of harmful MB. Furthermore, antibacterial activity was assessed against *E. coli* and *S. aureus*. To identify possible mechanism of action, molecular docking studies of Bi-doped BN nanosheets were performed against dihydrofolate reductase (DHFR) enzyme from Folate biosynthetic pathway alongside DNA gyrase from nucleic acid biosynthetic pathway belonging to both *E. coli* and *S. aureus*. The first-principles density functional theory calculations were performed to computed the stability structure, electronic and optical properties of pristine and Bi-doped BN nanosheet.

Methods

The current study was impact of Bi-doped BN nanosheets on electronic and optical properties using theoretical calculations and experiments: dye degradation, anti-bactericidal behavior and molecular docking analysis.

Experimental Details

BN bulk powder (98%), dimethylformamide (DMF) were procured from Sigma-Aldrich, Germany. Bismuth nitride pentahydrate $\text{Bi}(\text{NO}_3)_3 \cdot 5\text{H}_2\text{O}$ (98%) from BDH laboratory supplies Poole, UK. All received chemicals were utilized without purification treatment.

To produce BN nanosheets, liquid phase exfoliation of bulk BN was carried out. 200 mg of bulk BN powder was dissolved in DMF (50 ml) and stirred for 15 min. Subsequently, the dissolved solution was ultrasonicated for 12 h at 50 °C as illustrated in Fig. 1a. This ultrasonicated suspension was centrifuged at 3500 rpm for 20 min [46]. Collected nanosheets were doped with Bi using bismuth nitride pentahydrate $\text{Bi}(\text{NO}_3)_3 \cdot 5\text{H}_2\text{O}$ as a source of Bi using hydrothermal method. Various Bi dopant concentrations (2.5, 5, 7.5 and 10 wt%) were added in

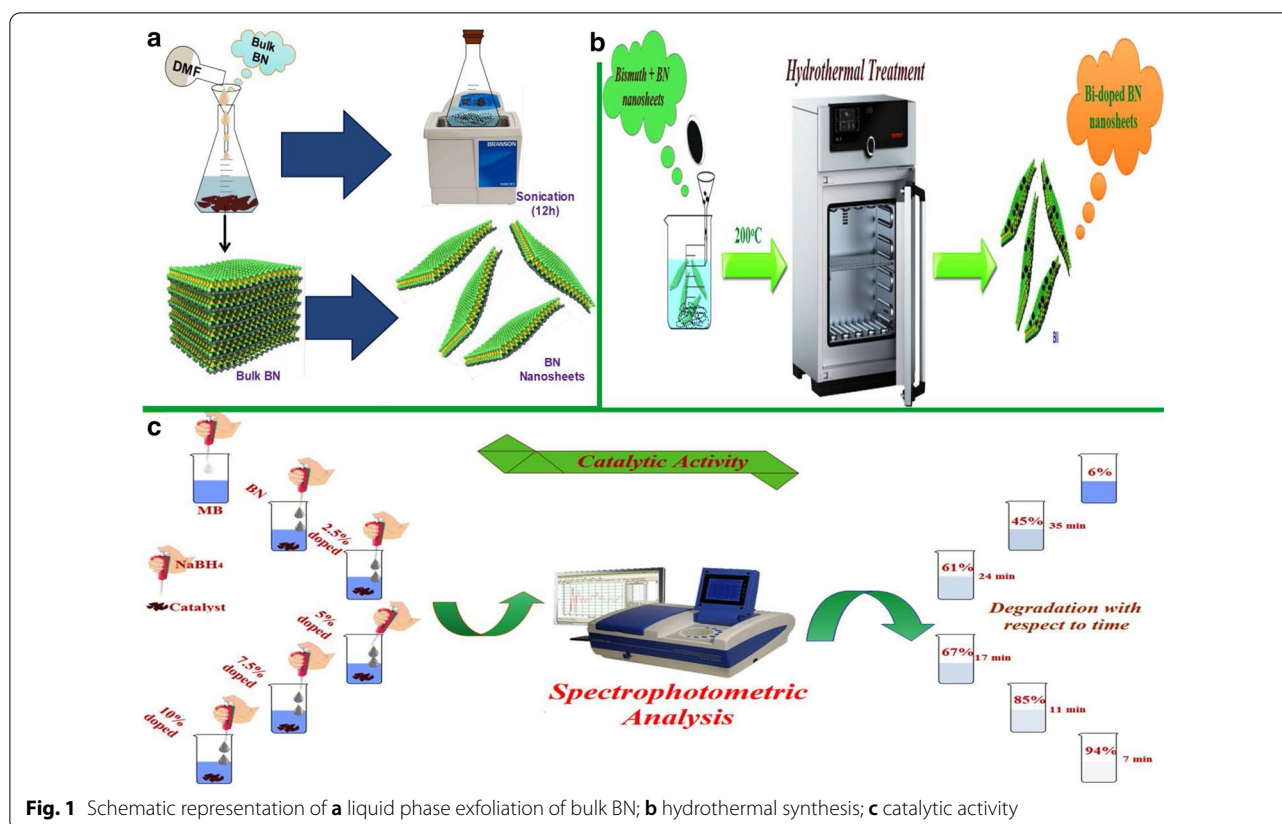


Fig. 1 Schematic representation of **a** liquid phase exfoliation of bulk BN; **b** hydrothermal synthesis; **c** catalytic activity

BN nanosheets separately at fixed ratios (0.025:1, 0.05:1, 0.075:1 and 0.1:1) in a Teflon vessel and transferred to autoclave for 12 h at 200 °C as shown in Fig. 1b. After that, autoclave was cool down and obtained product was washed repeatedly using cleaning agents such as ethanol and deionized water to eliminate impurities, and solution was dried at 100 °C in a vacuum oven.

Van der Waals attractions are the predominant forces among the stacked layers of bulk boron nitride. These Van der Waals interactions must be overcome to exfoliate stacked layers. This was performed using intercalation of organic solvent into layers followed by introduction of mechanical forces attained from ultra-bath sonicator. Solvents whose surface tension matches with that of boron nitride are the ideal solvents for well dispersion of bulk boron nitride, as they minimize the interfacial tension between the solvent and boron nitride. That is why we have adopted DMF as its surface tension is matches with graphene (37.1 m J m^{-2}) and BN is analogous to graphene so it is a quite suitable solvent to disperse boron nitride nanosheets [47].

Ultrasonic radiations travel through the medium, solvent molecules compress and stretch i.e. starts oscillating about their mean positions resulting in development of high pressure regions that can be named as compression

and negative pressure regions as stretching. When negative pressure is not large enough to hold liquid molecules intact, then breakdown of liquid takes place forming voids (cavitation bubbles). These cavitation bubbles will collapse violently in high pressure regions and behave like micro reactors, produce local temperature of several thousand degrees and high pressure of several hundred atmospheres which is sufficient to overcome the inter-sheet attractive forces and hence induces exfoliation [48, 49].

Catalytic Activity

Catalytic potential was evaluated by undertaking MB dye degradation in the presence of sodium borohydride (NaBH_4) which serves as reducing agent. Firstly, an appropriate amount of dye and reductant was diluted in deionized water to prepare an aqueous solution. Catalytic experiment was carried out by utilizing all prepared samples as nanocatalyst. Dye degradation was measured by adding NaBH_4 solution (600 μl) to MB (10 ml) in a quartz cell. It is worth mentioning here that NaBH_4 is unable to degrade the dye, therefore it serves as a reducing agent only. Furthermore, each catalyst (4 mg) was added separately into a precursor solution to investigate catalytic efficiency for dye degradation. Reduction of dye was

measured by taking absorption spectra in the range 450–750 nm with a UV–vis spectrophotometer. In this regard, decolorization of methylene blue is considered an indication of successful dye degradation. Schematic illustration of performed activity with pure BN and various doping concentrations is shown in Fig. 1c. The illustration to the left-hand side signifies performed activity while that to the right shows degradation concentration concerning the time after taking absorption spectra with UV–Vis spectroscopy.

Antimicrobial Activity

In-vitro assessment of antimicrobial potential of Bi-doped BNNS was accomplished through well diffusion method by swabbing 1.5×10^8 CFU/mL of G+ve and –ve bacterial isolates on MSA and MA, respectively as shown in Additional file 1: Fig. S1. Various ratios of Bi-doped BNNS (500 µg/50 µl) and (1000 µg/50 µl) were inoculated as low and high dose in wells (6 mm) on MSA and MA plates Additional file 1: Fig. S1. Ciprofloxacin (5 µg/50 µl) and DIW (50 µl) were labeled as positive (+ve) and negative (–ve) controls. Anti-bacterial evaluation was proven by inhibition zones (mm) measurements using Vernier caliper after overnight incubation of Petri dishes at 37 °C [50]

Materials Characterization

X-ray diffractometer (XRD) from Bruker (D₂ Phaser, USA) equipped with Cu-K α ($\lambda = 0.154$ nm) was used with diffraction angle (2θ) range from 10° to 60° with 0.05/min scan rate to determine the structural characteristics of synthesized material. Fourier transform infrared (FTIR) spectroscopy (Perkin Elmer spectrometer) with wave-number accuracy within ± 0.01 cm^{–1} was employed to outline IR fingerprints. Optical properties were evaluated using GENESYS-10S UV–Vis with a scan rate of 5 nm/s and absorption spectra range from 200–800 nm and photoluminescence study was undertaken with JASCO FP-8200 spectrofluorometer with scan rate 10 nm/s. Surface morphology and microstructure were studied using field emission scanning electron microscope (FESEM model JSM 6460LV) coupled with energy dispersive x-ray (EDS) spectrometer and JEOL JEM 2100F high-resolution transmission electron microscope (HR-TEM).

Computational Details

Our first-principles calculation was conducted by comprehensive framework of the DFT as implemented in the QuantumATK software [51] using local combination of the atomic orbitals (LCAO) approach. The exchange–correlation functional was conducted by Perdew, Burke, Ernzerhof (PBE) connecting with the generalized gradient approximation (GGA) [52]. The norm-conserving

PseudoDojo [53] pseudopotential was employed for describing the interaction between electrons and ions, and the valence electrons. The Brillouin region was performed employing Monkhorst–Pack's special k-point grid of $4 \times 4 \times 1$ for structural relaxation and $7 \times 7 \times 1$ for electronic property calculations. The calculation of self-consistent field (SCF) was taken into account a tolerance limit of 10^{-6} Ha for energy convergence. The geometry structure and ion relaxations were carried out by using the limited-memory Broyden–Fletcher–Goldfarb–Shanno (LBFGS) algorithm, including the force on each atom less than 0.05 eV/Å. On account of the strong relativistic effect owing to presence of heavy Bi dopant, spin-orbital coupling (SOC) contribution has been considered in the calculation of the electronic structures.

Results and Discussion

Structure and Electronic Properties

XRD was employed to investigate phase identification, crystallinity, and crystallographic planes of control and Bi-doped BN nanosheets as illustrated in Fig. 2a. The XRD reflections identified at 2θ values of $\sim 26.9^\circ$, 41.3° , 43.46° , and 50.2° were respectively indexed as (002), (100), (101), and (102) crystallographic planes. Detected crystallographic planes harmonized well to standard spectrum (JCPDS reference #00-034-0421) [54, 55]. Sharpness and peak intensity suggest formation of BN thin layers and weak stacking of NS in preferred c-direction [46]. Peak shift concerning diffraction angle was detected in XRD reflections, which suggests incorporation of dopant. Interlayer spacing (d -value) of characteristic (d_{002}) reflection was found ~ 0.34 nm as evaluated through Bragg's law ($n\lambda = 2d\sin\theta$) and correlates well with HR-TEM results (see Additional file 1: Fig. S4). This d -value of corresponding plane is characterized by significant features pertaining to adsorption properties and molecular transport of BN that serves to enhance its catalytic performance [56]. Corresponding SAED profiles of bare BN represented in Fig. 2b consist of bright circular rings that indicate high crystallinity of sample. These detected rings agree well with XRD patterns and standard data [26, 57, 58]. The surface morphology of the synthesized material was explored using FESEM and further confirmed through HR-TEM analysis. Interlayer spacing was evaluated with Gatan digital micrograph software using HR-TEM images, which was found to be consistent with XRD results. The purity of prepared product was ascertained by analyzing elemental composition through EDS spectroscopy as illustrated in Additional file 1: Figs. S5 and S6.

FTIR was employed to investigate IR fingerprints of host and Bi-doped BN nanosheets as shown in Fig. 2c. Obtained spectra display two characteristic

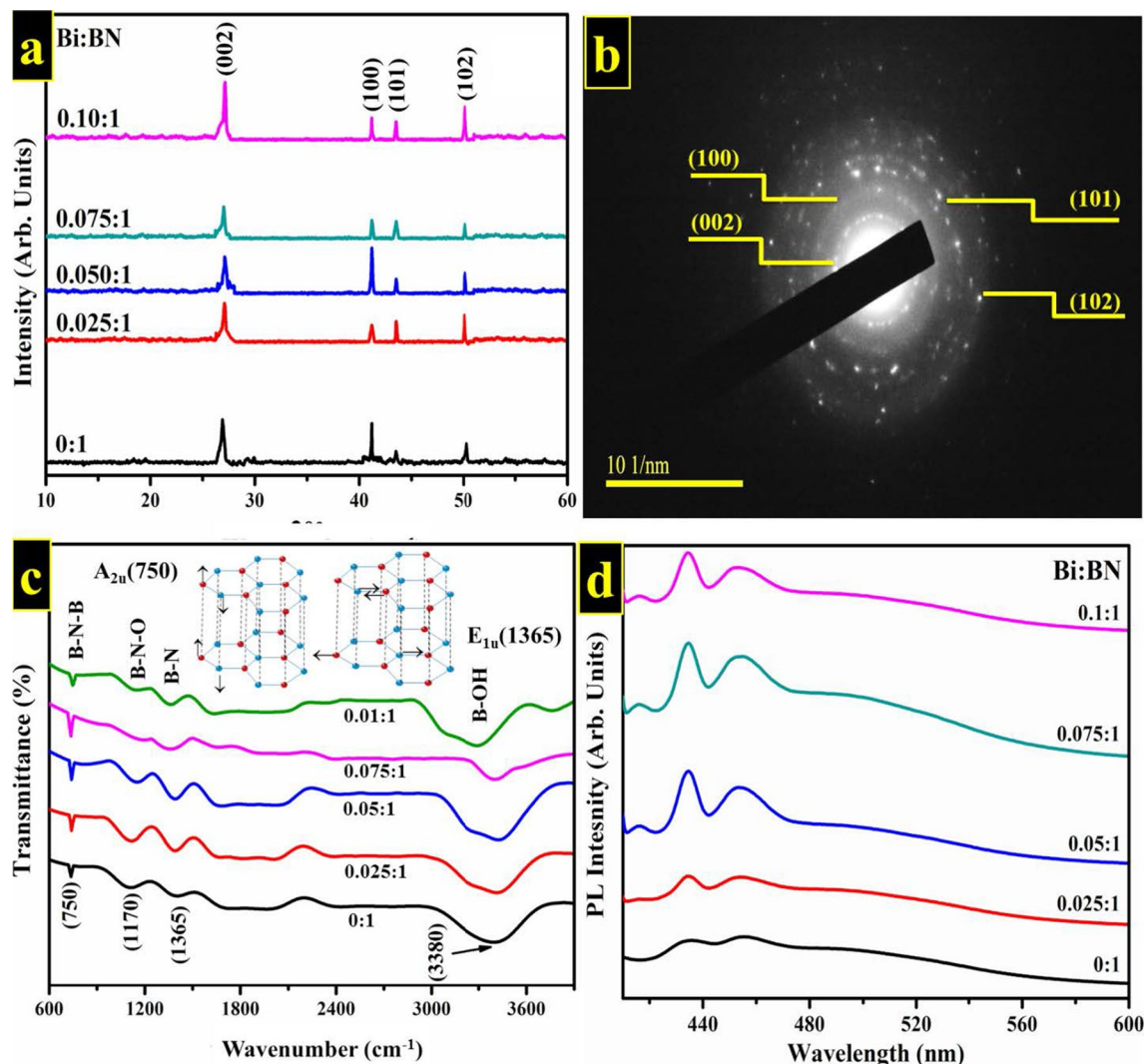


Fig. 2 **a** XRD patterns of host and Bi-doped BN nanosheets with various concentrations (2.5, 5, 7.5 and 10 wt%); **b** SAED pattern obtained from BN nanosheets; **c** FTIR spectra; **d** PL spectra

peaks originating from BN at 750 and 1365 cm^{-1} can be attributed to B–N–B (bending vibrations) as well as B–N (stretching vibration). These core peaks are related to A_{2u} mode (out-of-plane) as well as E_{1u} mode (in-plane) [56, 59]. As mentioned A_{2u} mode is an out-of-plane mode that corresponds to the energy of 96.4 meV, whilst the E_{1u} corresponds to in-plane modes that further splits into two modes first one is longitudinal optical mode of E_{1u}^{TO} and secondly transverse optical E_{1u}^{LO} with energies of 169.4 and 199.6 meV respectively, due to the long-range Coulomb interactions as pointed out by Michel and Verberck [60]. In their work, they compared two phonon dispersion relations that were calculated without and with the long range Coulomb force,

respectively. The change among the two calculations corresponds to LO-TO splitting. Owing to Coulomb interaction which breaks the symmetry field in BN leading to the divide the longitudinal and transverse optical phonons [61]. A schematic illustration of these modes is shown in Fig. 2c. An additional peak was detected at 1170 cm^{-1} is associated with the stretching vibration of boron oxynitride (N–B–O). Broad band at 3433 cm^{-1} corresponds to O–H stretching vibration [62].

PL spectroscopy was used to confirm the excitons migration, transfer, and recombination in samples as shown in Fig. 2d. Extracted spectra were marked with excitation wavelength i.e. $\lambda_{\text{ex}} = 390$ nm and corresponding emission wavelength $\lambda_{\text{em}} = 420$ nm. Since

nanoscale materials are relatively sensitive to excitation wavelength, emission spectra are based on the value of λ_{ex} [59]. PL spectra of undoped and Bi-doped BN nanosheets displayed asymmetric peaks located at ~ 420 nm onwards. These detected asymmetric peaks in PL spectra suggest the existence of luminescent species and/or multi-fluorophores. Literature studies suggest that the presence of species such as boron–oxygen is regarded as novel luminescence centers in BN system [63]. Luminescence founds around 460 nm represent electronic transition commencement. This electronic transition involves individual/mutual transition lies between 2p states of BN bands [64]. Excitation of an electron (e^-) from valance to conduction band serves to enhance intensity of luminescence and energy of excitation light. This transition at 460 nm corresponds to energy peak at ~ 2.7 eV [65]. It is worth mentioning that samples were prepared via same quantity, growth rates, as well as durations etc., but the somewhat difference in intensities of all the samples for PL spectra may be attributed to less h-BN domains per unit area that are taking part in luminescence [66]. Maximum recombination and separations of excitons correspond to highest and lowest intense peaks in PL spectra respectively [67].

Optical properties of host BN and Bi-doped BN nanosheets were ascertained through absorption spectra obtained using UV–Vis spectroscopy. Appearance of absorption in near UV region was observed as illustrated in Fig. 3a. The maximum absorption for pure BN nanosheets was detected around 200 nm which is known as near UV region that corresponds to the bandgap energy of ~ 5.85 eV. With the incorporation of Bi

the maximum absorption edge is moved towards higher wavelength that indicates the redshift in optical spectra that causes to reduce the bandgap energy. Bandgap energy was estimated using Tauc equation which is represented in Eq. 1. Tauc plot in as displayed in Fig. 3b represents bandgap energy is reduced upto 4.65 eV. Besides these, no additional absorption towards lower or higher energy level was detected for pure, 2.5, and 5% Bi-doped samples, which suggests the existence of dense structural defects. Whereas for 7.5 and 10% Bi-doped samples very minor absorption around 330 is observed that is also verified and explained in the simulated optical absorption spectra analysis (see Fig. 6) [62, 68, 69]. According to the literature, bulk BN exhibits bandgap energy of 5.2–5.4 eV while bi/multilayer nanosheets possess bandgap energy of 5.56–5.92 eV [26]. These observations suggest that as-prepared BN nanosheets possess bi/multilayers configuration. Bandgap energy of all samples displayed in Fig. 3b and estimated through Tauc Eq. (1) is expressed as follows:

$$\alpha h\nu = K(h\nu - E_g)^n \quad (1)$$

In the above equation, α indicates absorption coefficient which is equal to $\alpha = \log(T/d)$ where T is transmission and d is path length. Further, value of exponent (n) is associated with electronic nature of E_g and corresponds to direct allowed transitions (1/2), indirect allowed transitions (2), direct forbidden transitions (3/2) and indirect forbidden transitions (3), respectively. However, transition data allows to best linear fit in band edge area if $n = 1/2$. E_g is characteristically measured by assessing of $(\alpha h\nu)^{1/n}$ vs $h\nu$ plots. Linear trend acquired from Eq. 1 is modeled as the tangent of plot near point of maximum

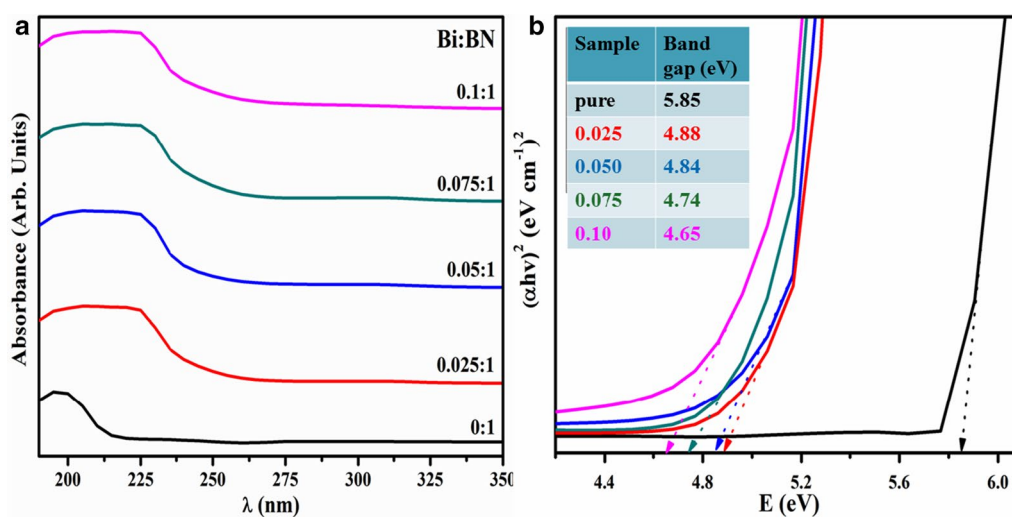


Fig. 3 **a** UV–Vis spectra of host and Bi-doped BN nanosheets; **b** bandgap energy analysis using Tauc plot

slope region. Here, $h\nu$ equals photon energy (E), K is absorption index and E_g is band gap energy (eV) [26].

These experimental findings are supported by first principle-based DFT calculations. The model of undoped and Bi-doped BN monolayers is built using the supercell method with periodic boundary conditions. A 7×7 supercell was used for pristine and Bi-doped BN monolayer to assure minimal interaction of Bi with its neighboring images. A 15 Å vacuum layer was used along the direction perpendicular to the plane of the monolayer. The dopant concentrations of 2.04%, 4.08%, and 6.1% have been modeled by substituting one, two, and three Bi atoms in the BN monolayer supercell at B sites, as shown in Additional file 1: Fig. S6. To examine the stability of Bi dopant with different concentration, we estimated the binding energies using the following equations [70, 71]:

$$E_b = E_{\text{supercell}} - E_V - E_{\text{TM}} \quad (2)$$

whereby, $E_{\text{supercell}}$, E_V , and E_{TM} refer to the total energy of the doped BN, host material with cation vacancy, and the isolated metal atom. It is found that the value of E_b for

different dopant concentrations changes strongly from -4.0 to -7.71 eV.

To explore the impact of Bi dopants on the change of the electronic structures and the optical behavior, we computed the electronic band structures and density of states (DOS) by including SOC contribution of Bi-doped BN monolayer with different concentrations as well as pristine BN monolayer for comparison, as shown in Figs. 5 and 6. It can be seen that pristine BN has direct bandgap energy of magnitude 4.69 eV at K point, as shown in Fig. 4a, which is more consistent with measured experimental value (5.85 eV). In addition, our computed bandgap energy value is excellent agreement with previous theoretical works [72, 73]. This bandgap energy value indicates that BN monolayer is an insulator. According to the plots of the DOSs of the pristine from Fig. 5a, the valence band maxima is mainly featured by the N 2p states whereas the minimum of the conduction band is mostly controlled by unoccupied B 2p states. When introducing a Bi dopant with doping level of 2.04%, two new localized gap states are formed around Fermi level, as shown in Fig. 4b, in which the lower band is occupied

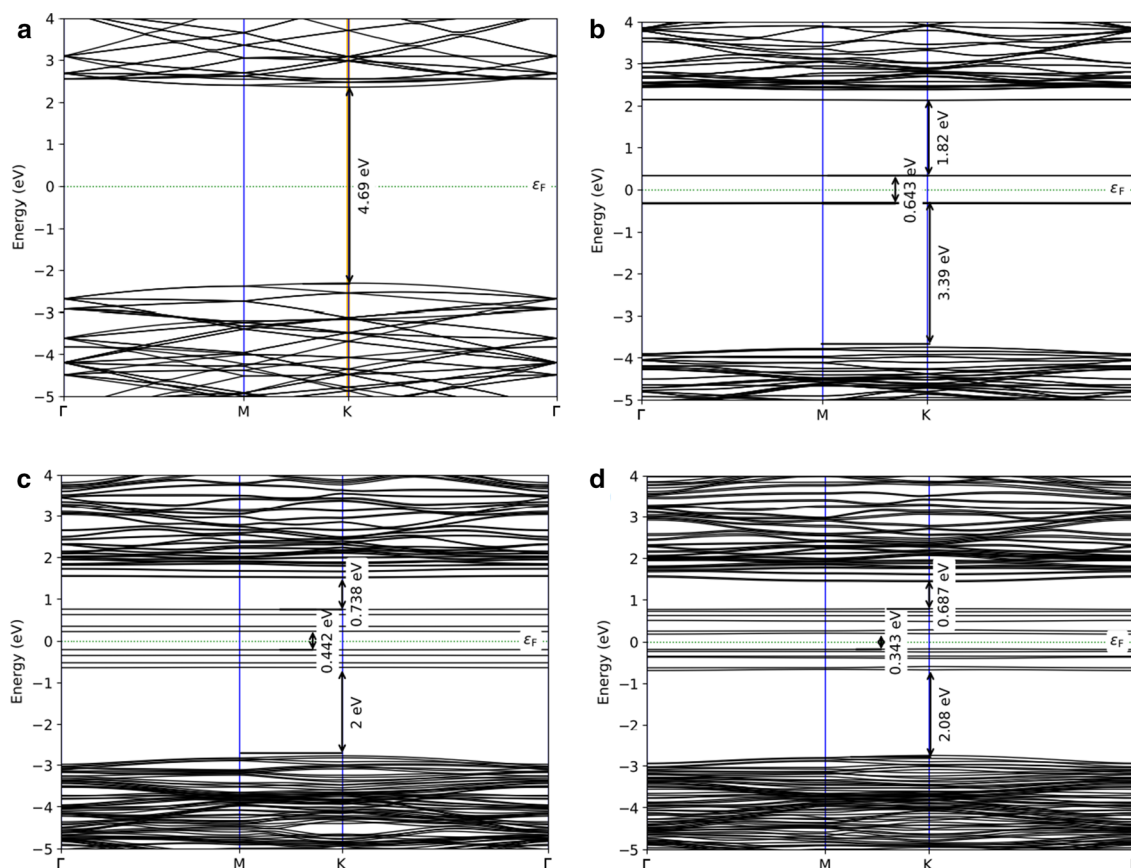


Fig. 4 The computed electronic band structure of **a** pristine BN and Bi-doped monolayers with concentrations **b** 2.04%, **c** 4.08%, and **d** 6.1%

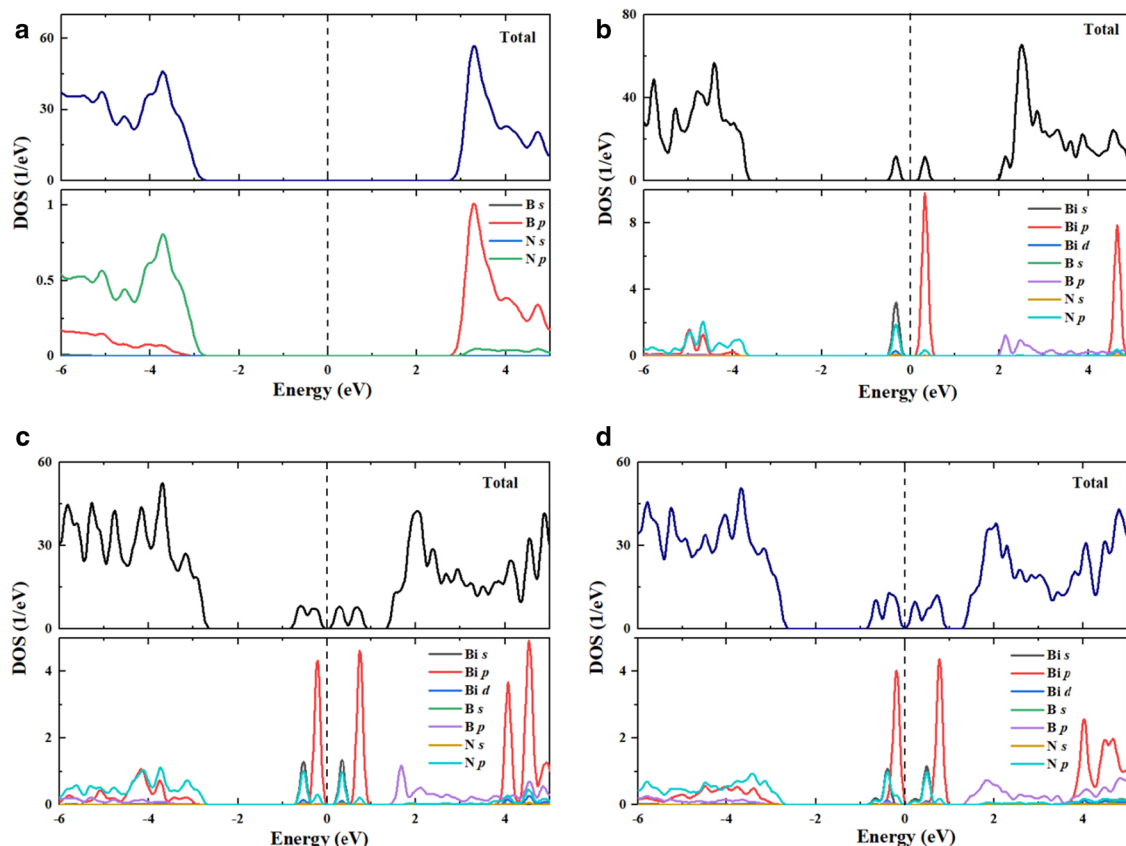


Fig. 5 Calculated total and projected DOS of **a** pristine BN and Bi-doped BN monolayers with concentrations, **b** 2.04%, **c** 4.08%, and **d** 6.1%

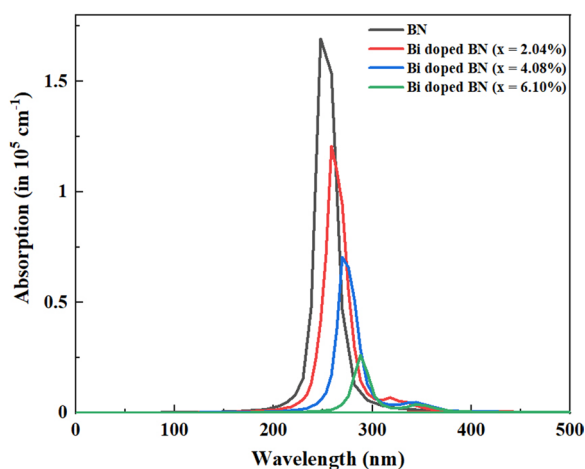


Fig. 6 The simulated optical absorption spectra of pure and Bi-doped BN monolayers

whereas the upper band is unoccupied. Therefore, the valence band maximum has been shifted to lower in the valence band reducing the bandgap energy. Moreover,

the main feature of the valence band maximum and conduction band minimum is similar to that of the pure BN monolayer. The appearance of impurity bands divides the bandgap energy into three energy sub-gap region having widths 3.39, 1.83 and 0.643 eV. The partial DOSs analysis (see Fig. 5b) reveals that the occupied gap states are mainly built up from Bi 6s states mixed with N 2p states while the unoccupied gap states are mainly owing to Bi 6p states with small contribution of N 2p states. In the case of two Bi atoms doping into BN monolayer, the band structure presents a relatively larger shift downward of the conduction band. It is noticed that the number of dopant bands are increased causing further reduction in bandgap energy. The result is that Bi-doped BN monolayer exhibits typical characters of n-type semiconductor. It follows from Fig. 4c that four gap states have been introduced around Fermi level. The lowest two dopant levels are occupied and located about 0.57 and 0.21 eV below the Fermi level. The other two-gap states are unoccupied and situated at 0.40 and 0.80 eV above the Fermi level. However, the PDOS in Fig. 5c shows a large part of hybridization between Bi 6s and N 2p states for two small peaks and a great contribution of Bi 6p states with

a small contribution of N $2p$ states for two high peaks. With increasing doping concentration of Bi at 6.1%, it is observed that more impurity states have been introduced around the Fermi level with reducing the band gap, as shown in Fig. 4d. The impurity bands with lower energy gap states occur at 0.36 eV while the impurity bands with higher energy gap states locate at 0.61 eV above the Fermi level. From the plot of partial DOS (see Fig. 5d), it can be perceived for Bi doping in BN at concentration of 6.1% that the main feature of impurity bands below and above the Fermi level is similar to that of the Bi-doped BN with $x=4.08\%$ with some overlapping between impurity bands below and above the Fermi level.

The absorption coefficients of pristine and Bi-doped BN monolayers are calculated and plotted in Fig. 6. It can be observed a redshift of the absorption edge with the increase of Bi doping concentration. In the Bi dopant concentration of 2.04%, the absorption edge shows a redshift of about 10 nm compared to that of pristine BN monolayer. This little redshift may appear from the slight bandgap energy decreasing and is in fair agreement with experimental measurement redshift of 20 nm for Bi doping into BN nanosheet. When the Bi incorporation concentration rising to 4.08% and 6.10%, the principal absorption edge has a more redshift about 22 nm and 40 nm compared with that of undoped BN monolayer. This has also resulted from the narrowing of bandgap energy, which leads to reproduce the experimental observation (see Fig. 3a). It can be observed that another very small absorption peak around 330 nm has appeared with the rise of Bi incorporation concentration. It further redshifts the absorption edge of the Bi-doped BN monolayer to a wavelength value of 345 nm (or energy of 3.60 eV), which signifies the enhancement of the catalytic ability.

Catalytic Activity

Results of experiments to evaluate performance of catalytic activity of the synthesized material are represented by utilizing time-dependent UV–Vis spectra. It was observed that incorporation of reductant into an aqueous solution of dye was unable to degrade it as only ~7% of dye reduction was achieved. Addition of Bi-doped into BN nanosheets (nanocatalyst), percentage degradation is effectively enhanced. Pure BN nanosheets display 45% dye reduction in 35 min while BN doped with various concentrations (2.5, 5, 7.5, and 10 wt%) of Bi exhibit enhanced dye reduction with rapid progress.

In general, catalyst lowers the activation energy of a reaction which in turn causes to accelerate its stability and rate of reaction. MB is primarily a synthetic dye that is exploited into water during various industrial processes. MB can be reduced in the presence of reductant however the reduction process is

relatively slow in the presence of only NaBH_4 . Host BN nanosheets exhibit large specific surface area causes to increase adsorption rate. Furthermore, a layer of reductant dispersed over nanocatalysts may also accelerate adsorption due to the redox reaction between catalyst and MB. Reduction reaction by a catalyst occurs by transferring an electron from donor species BH_4^- (from NaBH_4) to acceptor species MB facilitated by pure and Bi-doped BN nanosheets. This resulted to reduce activation energy which serves to stabilize and accelerate rate of the reaction [26, 74]. The mechanism of catalytic activity has been represented in Additional file 1: Fig. S7b. Dye degradation of various doped concentrations (2.5, 5, 7.5 and 10 wt%) was 61, 67, 85 and 94% in 24, 17, 11 and 7 min, respectively as illustrated in Fig. 7. The comparison of present experiment with literature is represented in Table 1.

Increase in the efficiency of catalytic activity is due to an increase in Bi concentration. As degradation percentage directly corresponds to the transfer of electrons from reducing agent towards MB which is facilitated by nanocatalyst. Bi-doped BN nanosheets cause to boost up the reaction rate by lowering its activation energy that in turn causes to facilitate transfer of electron more rapidly towards MB. Plot of C_t/C_o as a function of time represents dye reduction of all samples as illustrated in Fig. 7a where C_t represents concentration of MB at any given time while C_o corresponds to initial concentration. Figure 9b exhibits degradation percentage of catalysts which was estimated through Eq. 3.

$$\text{Degradation}(\%) = \frac{C_o - C_t}{C_o} \times 100 \quad (3)$$

Various factors that influence catalytic activity and affect the performance of catalysts are discussed below.

pH Value

In catalysis (catalytic activity), rate of reaction has a strong correlation with pH value. In general, an extremely low or high value of pH cannot contribute to dye degradation. Literature studies of catalytic activity using reducing agents demonstrate that rate of reaction at basic conditions is most favorable for maximum degradation. In the present study, the pH value at which the maximum degradation was attained was 8.4, which favorably correlates with literature cited. Further, materials such as BN nanosheets controls surface charge and dominate the possible electrostatic interaction between pollutant and material. Therefore, pH value of solution has direct linkage with removal process of pollutants by means of controlling the possible electrostatic interaction between the pollutant and adsorbent [74, 75].

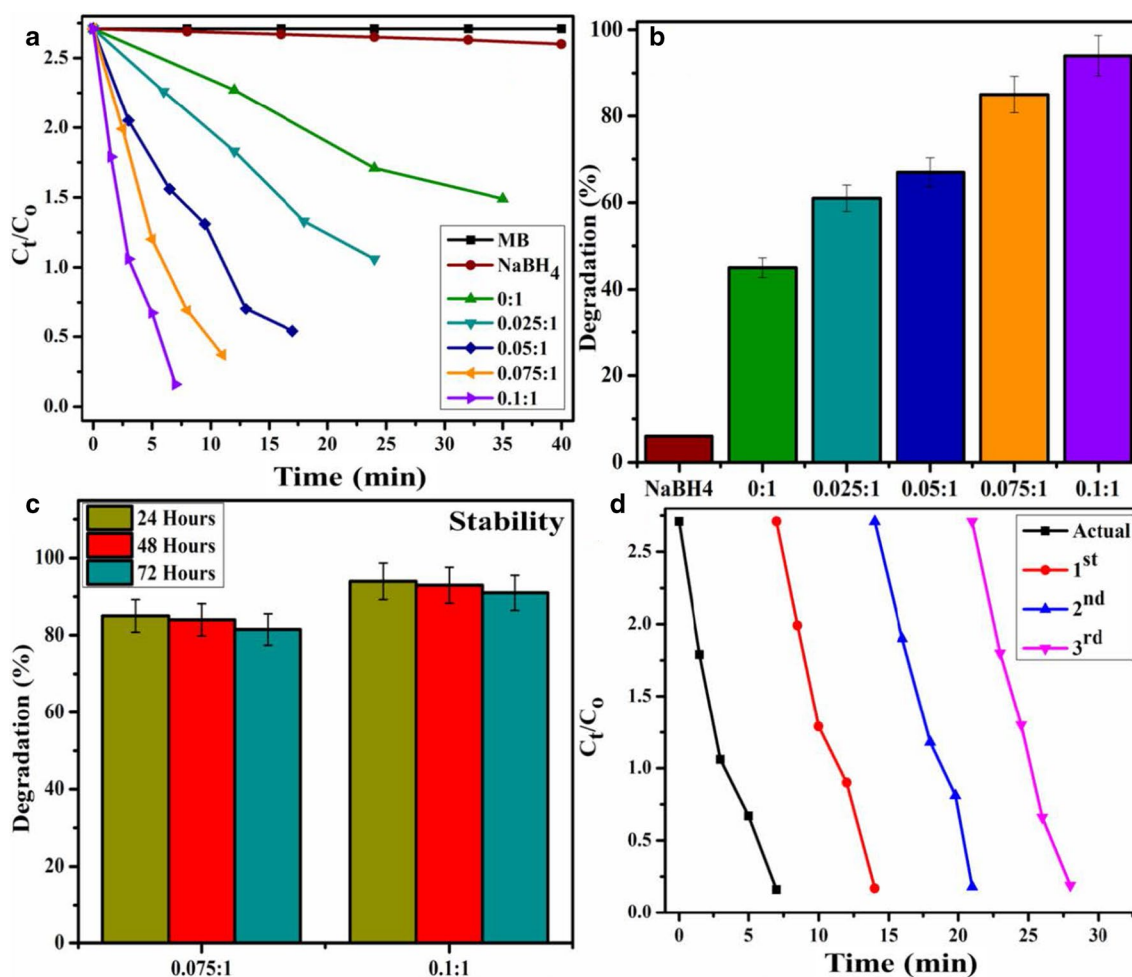


Fig. 7 **a** Plots of C_t/C_0 versus time for all catalysts; **b** comparison of degradation percentage over various concentrations, **c** comparison of stability for 7.5 and 10 wt% Bi-doped catalyst; **d** plot of C_t/C_0 versus time for reusability of 10 wt% Bi-doped BN catalyst

Table 1 Comparison of dye degradation with respect to reported literature

Reported	Samples	Type	Efficiency
Dan Liu et al. [76], Xiaomeng et al. [77]	BN/TiO ₂ hybrid nanosheetsAg ₃ PO ₄ /h-BN composite	Degradation of Rhodamine Bdegradation of MB	Maximum degradation in 6 h Maximum degradation in 50 min
Man Du et al. [78]	Co@BN	Reduction towards 4-nitrophenol	Maximum degradation in 22 min
Jia Yan et al. [79]	WO ₃ /h-BN nanocomposites	Degradation of Rhodamine B	Maximum degradation in 6 h
Present study	Bi-doped BN nanosheets	Degradation of MB	Maximum degradation in 7 min

Stability

The stability of catalyst was investigated in the present study by allowing performed experiment to stay for at least three days in order to examine whether the reduction of dye as performed in the presence of nanocatalyst is stable or not. In this regard degraded dye was

kept in dark and after every 24 h, degradation was inspected with the help of absorption spectra acquired through UV–Vis spectrophotometer, as illustrated in Fig. 7c. Obtained results indicate that no loss of degradation occurred in stay condition for 72 h. Degradation was observed to be in its fairly original form which affirms the stability of catalyst.

Reusability

Reusability of catalyst refers to recycling ability of catalyst that permits its use more than once. Typically, catalysts with the most number of reusable cycles are considered the most efficient catalyst. In the current experiment, reusability was probed by recycling 10 wt% catalyst up to three cycles. The obtained results are presented in Fig. 7d, which indicates Bi-doped BN catalyst can be utilized as an effective reusable catalyst.

Load of Catalyst

Lastly, load of catalyst before the experiment and after three times of recycling was found. Load of catalyst before performing activity was 4 mg, after three times recycling it was measured as 3.7 mg, considering 5% sensing/detecting deviation. The results indicated that Bi-doped BN acts as the most stable, reusable, and the most efficient dye degrading catalyst. Furthermore, a load of catalyst after three days stability test was also performed that indicate almost same result (3.6 mg) as performed after recycling process.

Bactericidal Activity

In-vitro bactericidal activity of BN, Bi_2O_3 , and Bi-doped BN nanosheets for Gram +ve and Gram -ve bacteria are shown with graphical presentations in Figs. 8 and 9 (a–n). The findings indicate superior bactericidal action with synergism of Bi-doped BN nanosheets against *E. coli* compared with *S. aureus* as shown in Figs. 8 and 9 (a–j). BN and Bi_2O_3 at low concentrations showed null efficiency against G +ve and -ve bacteria. At high concentrations, BN depicted (0.35 mm) and (0.45 mm) inhibition and similarly, Bi_2O_3 showed (0.55 mm) and (0.75 mm) zone of inhibition against G +ve and -ve bacteria respectively Figs. 8 and 9 (a, b, h–i). Significant ($P < 0.05$) inhibition zones were detailed as (0–2.45 mm) and (3.15–4.35 mm) for *S. aureus* and (0–1.65 mm) and (2.15–3.65 mm) for *E. coli* at low and high doses, respectively Figs. 8 and 9 (c–f, j–m). The efficiency percentage (% age) raised from (0–33.8%) and (43.4–60%) against *S. aureus* and (0–38.8%) and (50.5–85.8%) against *E. coli*, respectively. Ciprofloxacin used as positive control reduced (7.25 mm) and (4.25 mm) G+ve and -ve growth, respectively in comparison with DIW (0 mm). Generally,

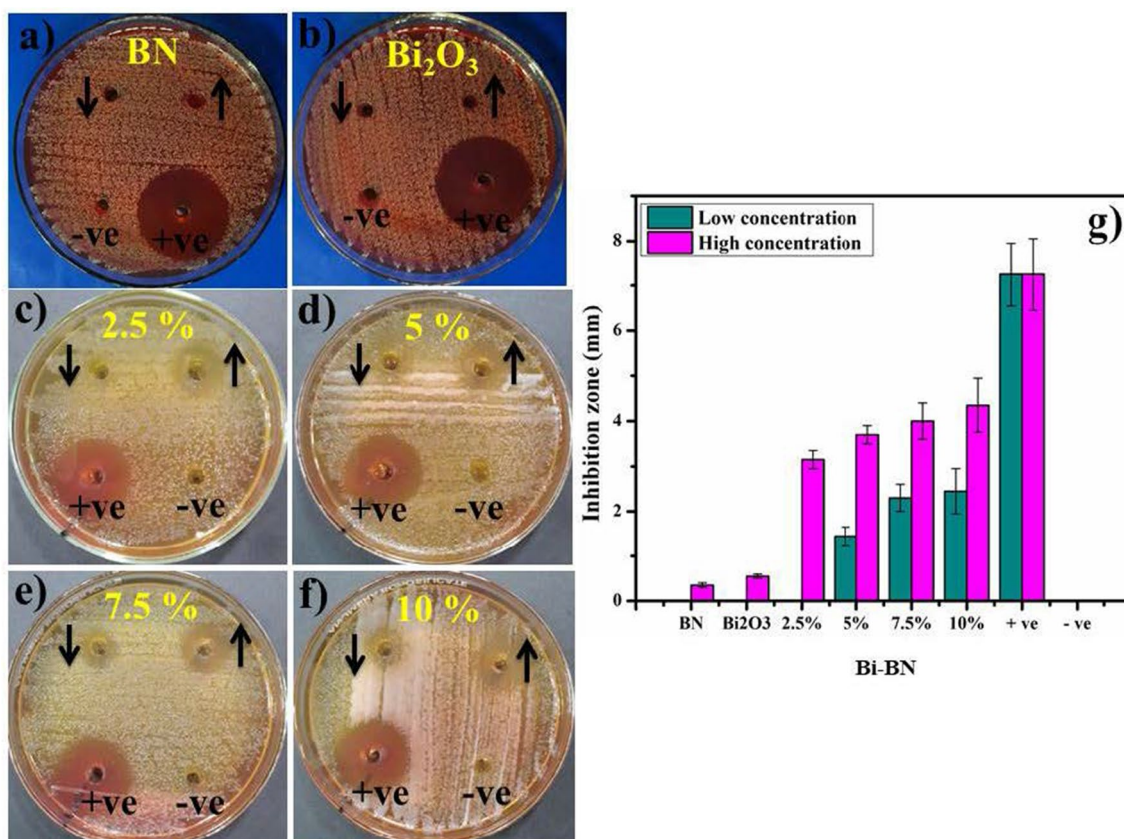


Fig. 8 a–g *In-vitro* antimicrobial efficiency of BN (a) Bi_2O_3 (b) BN nanosheets doped with various concentrations (2.5, 5, 7.5 and 10 wt%) of Bi against *S. aureus* (c–f) graphical presentation (g)

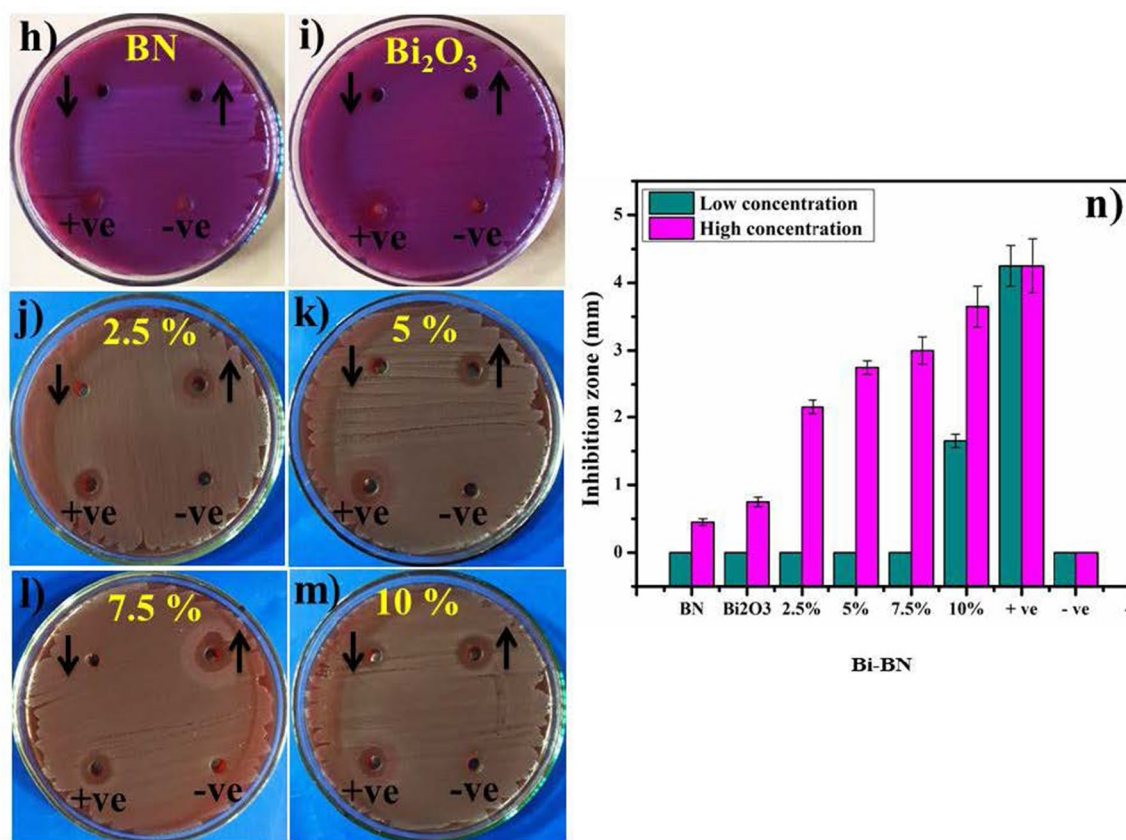


Fig. 9 h–n In-vitro antimicrobial efficiency of BN (h) Bi_2O_3 (i) BN nanosheets doped with various concentrations (2.5, 5, 7.5 and 10 wt%) of Bi against *E. coli* (j–m) graphical demonstration (n)

2.5 wt% doped BN nanosheets showed zero efficiencies against Gram +ve and -ve bacteria at low dose while, other doped nanosheets depicted significant ($P < 0.05$) antibacterial activity against Gram -ve compared to Gram +ve as shown in Figs. 8 and 9 (c–f, j–m).

The oxidative stress fashioned by nanosheets depends upon its size, shape, and concentration. Antibacterial activity with inhibition zones (mm) raised with greater wt% doping of Bi on BN due to more cationic availability. Antibacterial activity depending on size and concentration exhibited inverse relation to doped NS size [2, 22, 80]. ROS generation is considered a major hazardous factor for the destruction of micropathogens [81]. Small-sized NS produce reactive oxygen species (ROS) that stay more real within bacteria membrane within implants ensuing extrusion of cytoplasmic contents and damaging bacterial DNA, proteins, and enzymes thus, killing bacteria as illustrated in Additional file 1: Fig. S7 (a) [80, 82]. Upon irradiation, NPs activate e^- transfer from valence to conduction bands for reduction reactions by generating holes (h^+) which, ultimately transfer to valence band for oxidation [83,

84]. The reduction process generates O_2^- by reaction of e^- with O_2 [85]. The holes (h^+) via oxidation process generate OH through reaction with either e^- from water (H_2O) or hydroxyl ions (OH^-) [86]. The intense reactive oxygen radical species OH quickly reacts with micropathogens biomolecules i.e. proteins, carbohydrates, DNA, lipids and amino acids as shown in Additional file 1: Fig. S7 (a) [87]. Bismuth composites are famous for much effective antibacterial action coupled with low environmental toxicity [88]. Secondly, strong cationic interface of Bi^{+3} with negatively charged bacterial cell membrane parts grades in increased antibacterial action at high concentrations prompting bacteria collapse [2].

Enzyme catalyzing key steps of various biochemical reactions needed for bacterial survival represents attractive targets for antibiotic discovery. Molecular docking studies to predict inhibition tendency of nanoparticles against selected enzyme targets are of utmost importance for new antibiotic discovery. The mechanism of enzyme inhibition is depicted in Additional file 1: Fig. S7 (c) showing blockage of enzyme active site

that hinder substrate access and disrupt catalytic activity of given enzyme target causing bacterial death.

Although extensive literature is reported over biological potential of nanomaterials particularly, bactericidal activity still clear mechanism of their action is not known. Nanomaterials show their antibacterial activity either through cell wall rapturing or may target key enzymes of various pathways that are essential for bacterial survival (see Additional file 1: Fig. S7) [80, 89]. Identifying their target is of worth importance and may contribute towards discovery of new antibiotics with a novel mode of action [90]. Here, enzyme targets of two well-known antibiotics i.e. Rifampicin (Nucleic acid synthesis) and Trimethoprim (Folate biosynthetic pathway) [91] have been selected to evaluate binding tendency, binding interaction pattern, and inhibitory mechanism of Bi-doped BN nanosheets behind their antibacterial activity.

In case of DHFR from *E.coli*, the best-docked conformation showed H-bonding interaction with Ile14 (2.68 Å) and Ile94 (2.27 Å) alongside metal-contact interaction with Tyr100 having binding score as -11.971 kcal/mol (Fig. 10a). Similarly, H-bonding interaction with Thr46 (2.19 Å) and metal-contact with Leu20 was observed in case of DHFR from *S. aureus*

having binding score -8.526 kcal/mol as shown in Fig. 10b.

For DNA gyrase from *E.coli*, the best binding score observed was -6.782 kcal/mol having H-bonding interaction with Asp73 (2.22 Å) as shown in Fig. 11a while in case of DNA gyrase from *S. aureus* H-bonding interaction were observed with Asp81 (2.12 Å and 2.68 Å) alongside metal contact interaction with Ile175 having binding score -7.819 kcal/mol (Fig. 11b).

Conclusion

BN nanosheets were successfully prepared through liquid-phase exfoliation of bulk BN while Bi was incorporated as dopant via hydrothermal approach. Various properties of synthesized material were studied using number of characterization approaches that are well harmonized with literature. XRD patterns indicated the presence of hexagonal phase of BN with peak shift to higher diffraction angle, which authenticates successful incorporation of dopant. FTIR spectra affirm the presence of in-plane B–N bending and out-of-plane B–N–B stretching vibrations, which corresponds to the presence of infrared active E_{1u} and A_{2u} modes of BN. The presence of luminescence band was affirmed through PL analysis whereas UV–Vis spectroscopy indicates the occurrence

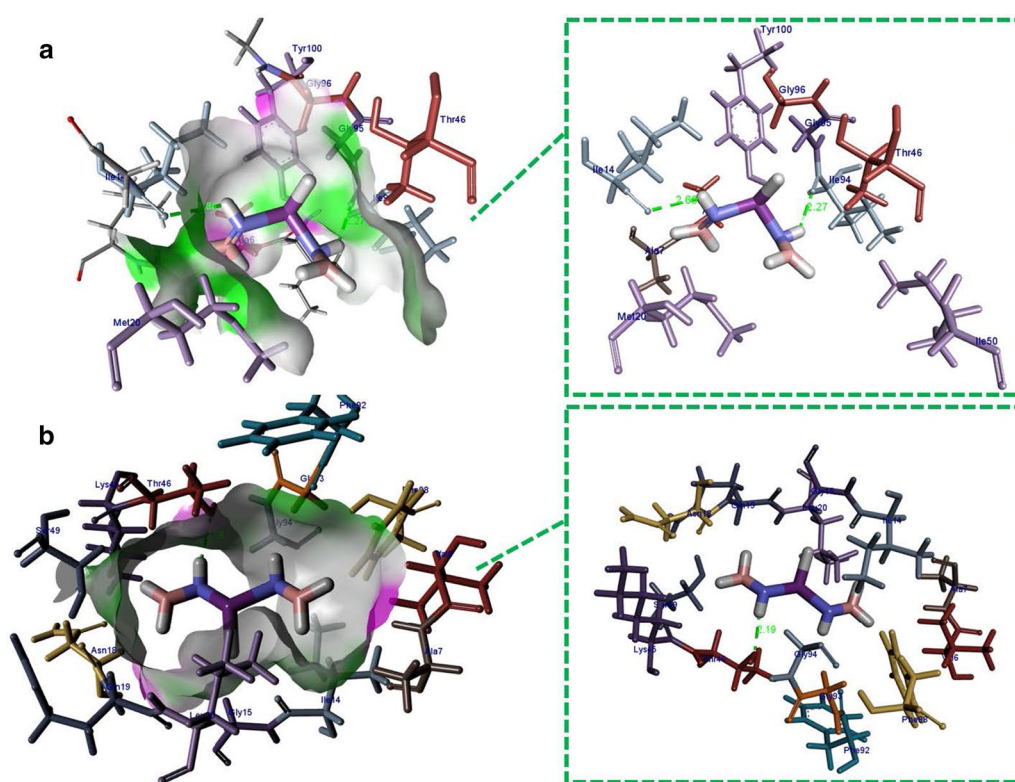


Fig. 10 Binding interaction pattern of Bi-doped BN nanosheets with active site residues of dihydrofolate reductase from **a** *E. coli* and **b** *S. aureus*

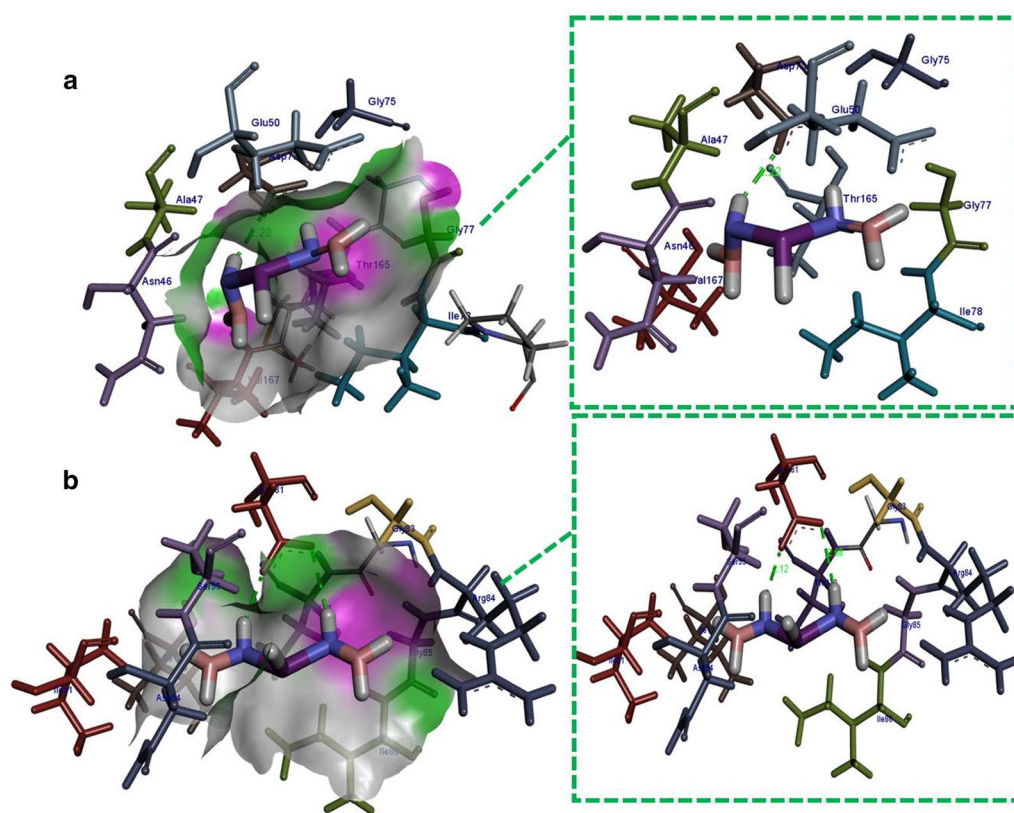


Fig. 11 Binding interaction pattern of Bi-doped BN nanosheets with active site residues of DNA gyrase from (a) *E. coli* and (b) *S. aureus*

of absorption in near UV region. Morphological examinations were studied via FESEM and HR-TEM micrographs indicated sheet-like morphology with decoration of Bi over nanosheets, which signifies an effective doping procedure. Interlayer spacing estimated through HR-TEM images with the aid of Gatan digital micrograph software that corresponds well with XRD; while EDS spectra showed strong signals originating from both pure as well as dopant material. The optimization results from the first principle calculation reveal that Bi can be substituted and stable into BN nanosheets with different concentrations. Impurity bands due to Bi atoms introduce a sub-bandgap energy absorption in the electronic bandgap energy region which might increase the catalytic activity. Investigation of dye degradation via CA experiments resulted in an efficient and rapid process. Further pure and doped BN nanosheets serve as stable, reusable, and outstanding nanocatalyst for wastewater treatment. In addition, antimicrobial efficiency of doped BN nanosheets against *S. aureus* and *E. coli* isolated directly from caprine mastitic milk resulted in significant quantitative values. In silico predictions against selected

enzyme targets i.e. DHFR and DNA gyrase from *E. coli* and *S. aureus* were in good agreement with in-vitro bactericidal activity thereby, opening a new horizon for the use of doped nanomaterials as potential agents for antimicrobial and CA procedures. Theoretical calculations are in good agreement with experimental values. Theoretical study indicates that substitutional doping of Bi with different concentrations is stable. Moreover, Bi doping led to various modifications in the electronic structures of BN nanosheets by inducing new localized gap states around the Fermi level. Finally, upon these results, it can be concluded that Bi-doped BN nanosheets is a suitable material to utilize in industrial wastewater applications, and antimicrobial treatment.

Abbreviations

Bi: Bismuth; BN: Boron nitride; EDS: Energy-dispersive X-ray spectroscopy; FESEM: Field emission scanning electron microscopy; FTIR: Fourier transform infrared spectroscopy; G+ve: Gram-positive; G-ve: Gram-negative; HR-TEM: High-resolution transmission electron microscope; JCPDS: Joint Committee on Powder Diffraction Standards; MA: MacConkey agar; MB: Methylene blue; nm: Nanometer; PL: Photoluminescence; UV-Vis: Ultra-violet visible spectroscopy; XRD: X-ray diffraction.

Supplementary Information

The online version contains supplementary material available at <https://doi.org/10.1186/s11671-021-03542-x>.

Additional file 1. Supplementary Materials.

Acknowledgements

Authors are thankful to the Center for Engineering Research, Research Institute, King Fahd University of Petroleum & Minerals, Dhahran, Saudi Arabia for HR-TEM analysis. The authors are also grateful to MOU signed authorities between GC University and Riphah International University Lahore Campus.

Authors' contributions

MI provided the novel idea to carry out the experiment. MW performed the whole experiment and JH wrote the manuscript. AH performed antimicrobial activity and JH and SN participated in molecular docking analysis. AUH reviewed the manuscript, corrected the English, and carried out the FESEM and HRTEM analysis. SA reviewed the manuscript and corrected the English. SGS and MBK performed theoretical calculation. All authors read and approved the final manuscript.

Funding

Authors are thankful to Higher Education Commission Pakistan for financial support through SRGP-21–1669.

Availability of Data and Materials

All data are fully available without restriction.

Declarations

Competing interests

The authors declare that they have no competing interests.

Author details

¹Solar Cell Applications Research Lab, Department of Physics, Government College University Lahore, Lahore 54000, Punjab, Pakistan. ²Department of Physics, Riphah Institute of Computing and Applied Sciences (RICAS), Riphah International University, 14 Ali Road, Lahore, Pakistan. ³Department of Clinical Medicine and Surgery, University of Veterinary and Animal Sciences Lahore, Lahore 54000, Punjab, Pakistan. ⁴Tianjin Institute of Industrial Biotechnology, Chinese Academy of Sciences, Tianjin 300308, China. ⁵Core Research Facilities, King Fahd University of Petroleum and Minerals, Dhahran 31261, Saudi Arabia. ⁶College of Science, Physics Department, Alfaisal University, P.O. Box 50927, Riyadh 11533, Saudi Arabia. ⁷Department of Physics, College of Science, King Faisal University, P.O. Box 400, Al-Ahsa 31982, Saudi Arabia.

Received: 23 February 2021 Accepted: 3 May 2021

Published online: 12 May 2021

References

- Agenson KO, Oh J-I, Urase T (2003) Retention of a wide variety of organic pollutants by different nanofiltration/reverse osmosis membranes: controlling parameters of process. *J Membr Sci* 225(1):91–103
- Haider A et al (2020) Enhanced bactericidal action and dye degradation of spicy roots' extract-incorporated fine-tuned metal oxide nanoparticles. *Appl Nanosci* 10(4):1095–1104
- Wei G, Yu H, Quan X, Chen S, Zhao H, Fan X (2014) Constructing all carbon nanotube hollow fiber membranes with improved performance in separation and antifouling for water treatment. *Environ Sci Technol* 48(14):8062–8068
- Ahmadipour M, Arjmand M, Thirmizir MZA, Le AT, Chiam SL, Pung S-Y (2020) Synthesis of core/shell-structured $\text{CaCu}_3\text{Ti}_4\text{O}_{12}/\text{SiO}_2$ composites for effective degradation of rhodamine B under ultraviolet light. *J Mater Sci Mater Electron* 31(22):19587–19598
- Peng Q et al (2016) Cadmium removal from aqueous solution by a deionization supercapacitor with a birnessite electrode. *ACS Appl Mater Interfaces* 8(50):34405–34413
- Ahmadipour M, Arjmand M, Ahmad ZA, Pung S-Y (2020) Photocatalytic degradation of organic dye by sol-gel-synthesized $\text{CaCu}_3\text{Ti}_4\text{O}_{12}$ powder. *J Mater Eng Perform* 29(3):2006–2014
- Raza A et al (2020) Enhanced industrial dye degradation using Co doped in chemically exfoliated MoS_2 nanosheets. *Appl Nanosci* 10(5):1535–1544
- Raza A et al (2020) A comparative study of dirac 2D materials, TMDCs and 2D insulators with regard to their structures and photocatalytic/sono-photocatalytic behavior. *Appl Nanosci* 10(10):3875–3899
- Ikram M et al (2020) Dye degradation performance, bactericidal behavior and molecular docking analysis of Cu-doped TiO_2 nanoparticles. *RSC Adv* 10(41):24215–24233. <https://doi.org/10.1039/D0RA04851H>
- Ahmadipour M et al (2021) Photodegradation of rhodamine B-dye pollutant using $\text{CaCu}_3\text{Ti}_4\text{O}_{12}$ -multiwall carbon nanotube nanocomposites. *J Environ Chem Eng* 9(3):105185
- Shakoor S, Nasar A (2017) Adsorptive treatment of hazardous methylene blue dye from artificially contaminated water using *Cucumis sativus* peel waste as a low-cost adsorbent. *Groundw Sustain Dev* 5:152–159
- Ahmadipour M, Ain MF, Ahmad ZA (2017) Effects of annealing temperature on the structural, morphology, optical properties and resistivity of sputtered CCTO thin film. *J Mater Sci Mater Electron* 28(17):12458–12466
- Štandeker S, Veronovski A, Novak Z, Knez Ž (2011) Silica aerogels modified with mercapto functional groups used for Cu(II) and Hg(II) removal from aqueous solutions. *Desalination* 269(1):223–230
- Hegazi HA (2013) Removal of heavy metals from wastewater using agricultural and industrial wastes as adsorbents. *HBRC J* 9(3):276–282
- Ali M et al (2020) Preparation of Co and Ni doped ZnO nanoparticles served as encouraging nano-catalytic application. *Mater Res Express* 6(12):1250
- Ahmadipour M, Arjmand M, Ain MF, Ahmad ZA, Pung S-Y (2019) Effect of Ar:N₂ flow rate on morphology, optical and electrical properties of CCTO thin films deposited by RF magnetron sputtering. *Ceram Int* 45(12):15077–15081
- Indana MK, Gangapuram BR, Dadigala R, Bandi R, Guttena V (2016) A novel green synthesis and characterization of silver nanoparticles using gum tragacanth and evaluation of their potential catalytic reduction activities with methylene blue and Congo red dyes. *J Anal Sci Technol* 7(1):19
- Khasawneh OFS, Palaniandy P, Ahmadipour M, Mohammadi H, Bin Hamdan MR (2021) Removal of acetaminophen using Fe_2O_3 - TiO_2 nanocomposites by photocatalysis under simulated solar irradiation: optimization study. *J Environ Chem Eng* 9(1):104921
- Dervin S, Dionysiou DD, Pillai SC (2016) 2D nanostructures for water purification: graphene and beyond. *Nanoscale* 8(33):15115–15131. <https://doi.org/10.1039/C6NR04508A>
- Ikram M, Khan MI, Raza A, Imran M, Ul-Hamid A, Ali S (2020) Outstanding performance of silver-decorated MoS_2 nanopetals used as nanocatalyst for synthetic dye degradation. *Phys E Low-Dimens Syst Nanostruct* 124:114246
- Ikram M et al (2020) Promising performance of chemically exfoliated Zr-doped MoS_2 nanosheets for catalytic and antibacterial applications. *RSC Adv* 10(35):20559–20571
- Qumar U et al (2020) Synergistic effect of Bi-doped exfoliated MoS_2 nanosheets on their bactericidal and dye degradation potential. *Dalton Trans* 49(16):5362–5377. <https://doi.org/10.1039/D0DT00924E>
- Balasubramaniam B, Singh N, Kar P, Tyagi A, Prakash J, Gupta RK (2019) Engineering of transition metal dichalcogenide-based 2D nanomaterials through doping for environmental applications. *Mol Syst Des Eng* 4(4):804–827. <https://doi.org/10.1039/C8ME00116B>
- Ikram M et al (2020) Bactericidal behavior of chemically exfoliated boron nitride nanosheets doped with zirconium. *Appl Nanosci* 10(7):2339–2349
- Ikram M et al (2020) Evaluation of antibacterial and catalytic potential of copper-doped chemically exfoliated boron nitride nanosheets. *Ceram Int* 46(13):21073–21083
- Hassan J, Ikram M, Ul-Hamid A, Imran M, Aqeel M, Ali S (2020) Application of chemically exfoliated boron nitride nanosheets doped with Co to remove organic pollutants rapidly from textile water. *Nanoscale Res Lett* 15(1):75

27. Ahmadipour M, Ain MF, Goutham S, Ahmad ZA (2018) Effects of deposition time on properties of $\text{CaCu}_3\text{Ti}_4\text{O}_{12}$ thin film deposited on ITO substrate by RF magnetron sputtering at ambient temperature. *Ceram Int* 44(15):18817–18820
28. Odularu AT (2020) Bismuth as smart material and its application in the ninth principle of sustainable chemistry. *J Chem* 2020:9802934
29. Nagay BE et al (2019) Visible-light-induced photocatalytic and antibacterial activity of TiO_2 codoped with nitrogen and bismuth: new perspectives to control implant-biofilm-related diseases. *ACS Appl Mater Interfaces* 11(20):18186–18202
30. Song Y et al (2018) Multifunctional bismuth oxychloride/mesoporous silica composites for photocatalysis, antibacterial test, and simultaneous stripping analysis of heavy metals. *ACS Omega* 3(1):973–981
31. Chiam S-L, Soo Q-Y, Pung S-Y, Ahmadipour M (2021) Polycrystalline TiO_2 particles synthesized via one-step rapid heating method as electrons transfer intermediate for Rhodamine B removal. *Mater Chem Phys* 257:123784
32. Ikram M et al (2020) Photocatalytic and bactericidal properties and molecular docking analysis of TiO_2 nanoparticles conjugated with Zr for environmental remediation. *RSC Adv* 10(50):30007–30024. <https://doi.org/10.1039/D0RA05862A>
33. Usman Qet al. (2021) Silver decorated 2D nanosheets of GO and MoS_2 serve as nanocatalyst for water treatment and antimicrobial applications as ascertained with molecular docking evaluation. *Nanotechnology*
34. Saleem S, Ahmed B, Khan MS, Al-Shaeri M, Musarrat J (2017) Inhibition of growth and biofilm formation of clinical bacterial isolates by NiO nanoparticles synthesized from Eucalyptus globulus plants. *Microb Pathog* 111:375–387
35. Ahmed B et al (2017) Mitochondrial and chromosomal damage induced by oxidative stress in Zn^{2+} ions, ZnO -Bulk and ZnO -NPs treated *Allium cepa* roots. *Sci Rep* 7(1):40685
36. Hawkey PM (2008) The growing burden of antimicrobial resistance. *J Antimicrob Chemother* 62(suppl_1):i1–i9
37. Ahmed B, Solanki B, Zaidi A, Khan MS, Musarrat J (2019) Bacterial toxicity of biomimetic green zinc oxide nanoantibiotic: insights into ZnONP uptake and nanocolloid–bacteria interface. *Toxicol Res* 8(2):246–261
38. M. D. Manhart, "In Vitro Antimicrobial Activity of Bismuth Subsalicylate and Other Bismuth Salts," *Reviews of Infectious Diseases*, vol. 12, no. Supplement_1, pp. S11–S15, 1990.
39. Varposhti M, Abdi Ali A, Mohammadi P (2014) Synergistic effects of bismuth thiols and various antibiotics against *Pseudomonas aeruginosa* biofilm. *Jundishapur J Microbiol* 7(3):e9142–e9142 ((in eng))
40. Long X, Chen Q, Yu L, Liang X, Liu W, Lu H (2018) Bismuth improves efficacy of proton-pump inhibitor clarithromycin, metronidazole triple *Helicobacter pylori* therapy despite a high prevalence of antimicrobial resistance. *Helicobacter* 23(3):e12485. <https://doi.org/10.1111/hel.12485>
41. Fu X, Shen Y, Jiang X, Huang D, Yan Y (2011) Chitosan derivatives with dual-antibacterial functional groups for antimicrobial finishing of cotton fabrics. *Carbohydr Polym* 85(1):221–227
42. Ramos AA, Azqueta A, Pereira-Wilson C, Collins AR (2010) Polyphenolic compounds from salvia species protect cellular DNA from oxidation and stimulate DNA repair in cultured human cells. *J Agric Food Chem* 58(12):7465–7471
43. Ali K et al (2019) Comparative in situ ROS mediated killing of bacteria with bulk analogue, Eucalyptus leaf extract (ELE)-capped and bare surface copper oxide nanoparticles. *Mater Sci Eng C* 100:747–758
44. Ikram M et al (2020) Bimetallic Ag/Cu incorporated into chemically exfoliated MoS_2 nanosheets to enhance its antibacterial potential: in silico molecular docking studies. *Nanotechnology* 31(27):275704
45. Altaf S et al (2020) Synthesis and characterization of binary selenides of transition metals to investigate its photocatalytic, antimicrobial and anticancer efficacy. *Appl Nanosci* 10(7):2113–2127
46. Zhang B et al (2017) High-efficient liquid exfoliation of boron nitride nanosheets using aqueous solution of alkanolamine. *Nanoscale Res Lett* 12(1):596
47. Kaur A, Singh RC (2017) Managing the degree of exfoliation and number of graphene layers using probe sonication approach. *Fullerenes Nanotubes Carbon Nanostruct* 25(5):318–326
48. Ye H, Lu T, Xu C, Han B, Meng N, Xu L (2018) Liquid-phase exfoliation of hexagonal boron nitride into boron nitride nanosheets in common organic solvents with hyperbranched polyethylene as stabilizer. *Macromol Chem Phys* 219(6):1700482. <https://doi.org/10.1002/macp.201700482>
49. Wang Z et al (2016) Fabrication of boron nitride nanosheets by exfoliation. *Chem Rec* 16(3):1204–1215. <https://doi.org/10.1002/tcr.201500302>
50. Haider A et al (2020) Green synthesized phytochemically (*Zingiber officinale* and *Allium sativum*) reduced nickel oxide nanoparticles confirmed bactericidal and catalytic potential. *Nanoscale Res Lett* 15(1):50
51. Smidstrup S et al (2019) QuantumATK: an integrated platform of electronic and atomic-scale modelling tools. *J Phys Condens Matter* 32(1):015901
52. Perdew JP, Burke K, Ernzerhof M (1996) Generalized gradient approximation made simple. *Phys Rev Lett* 77(18):3865–3868
53. van Setten MJ et al (2018) The PseudoDojo: training and grading a 85 element optimized norm-conserving pseudopotential table. *Comput Phys Commun* 226:39–54
54. Q. Zhang, Z. Li, X. Li, L. Yu, and Z. Wu, "Boron nitride nanosheets decorated by bismuth ferrite particles: preparation, characterization, and effect on flame-retardant performance of epoxy resin," *Materials Research Express*, vol. 5, no. 9, p. 095019, 2018.
55. Guerra V, Wan C, Degirmenci V, Sloan J, Presvytis D, McNally T (2018) 2D boron nitride nanosheets (BNNS) prepared by high-pressure homogenisation: structure and morphology. *Nanoscale* 10(41):19469–19477. <https://doi.org/10.1039/C8NR06429F>
56. Tang CY, Zulhairun AK, Wong TW, Alireza S, Marzuki MSA, Ismail AF (2019) Water transport properties of boron nitride nanosheets mixed matrix membranes for humic acid removal. *Heliyon* 5(1):e01142
57. Ahmadipour M, Cheah WK, Ain MF, Rao KV, Ahmad ZA (2018) Effects of deposition temperatures and substrates on microstructure and optical properties of sputtered CCTO thin film. *Mater Lett* 210:4–7
58. Ahmadipour M, Ayub SN, Ain MF, Ahmad ZA (2017) Structural, surface morphology and optical properties of sputter-coated $\text{CaCu}_3\text{Ti}_4\text{O}_{12}$ thin film: Influence of RF magnetron sputtering power. *Mater Sci Semicond Process* 66:157–161
59. Ding Y, Torres-Davila F, Khater A, Nash D, Blair R, Tetard L (2018) Defect engineering in Boron Nitride for catalysis. *MRS Commun* 8(3):1236–1243
60. Michel KH, Verberck B (2011) Phonon dispersions and piezoelectricity in bulk and multilayers of hexagonal boron nitride. *Phys Rev B* 83(11):115328
61. Kim KK et al (2012) Synthesis of monolayer hexagonal boron nitride on Cu foil using chemical vapor deposition. *Nano Lett* 12(1):161–166
62. Kumar V, Nikhil K, Roy P, Lahiri D, Lahiri I (2016) Emergence of fluorescence in boron nitride nanoflakes and its application in bioimaging. *RSC Adv* 6(53):48025–48032. <https://doi.org/10.1039/C6RA05288F>
63. Umrao S et al (2019) Anticarcinogenic activity of blue fluorescent hexagonal boron nitride quantum dots: as an effective enhancer for DNA cleavage activity of anticancer drug doxorubicin. *Mater Today Bio* 1:100001
64. Doll GL, Speck JS, Dresselhaus G, Dresselhaus MS, Nakamura K, Tanuma SI (1989) Intercalation of hexagonal boron nitride with potassium. *J Appl Phys* 66(6):2554–2558
65. Wu W, Lv X, Wang J, Xie J (2017) Integrating AgI/AgBr biphasic heterostructures encased by few layer h-BN with enhanced catalytic activity and stability. *J Colloid Interface Sci* 496:434–445
66. Laleyan DA, Mengle K, Zhao S, Wang Y, Kioupakis E, Mi Z (2018) Effect of growth temperature on the structural and optical properties of few-layer hexagonal boron nitride by molecular beam epitaxy. *Opt Express* 26(18):23031–23039
67. Silly MG et al (2007) Luminescence properties of hexagonal boron nitride: cathodoluminescence and photoluminescence spectroscopy measurements. *Phys Rev B* 75(8):085205
68. Mahdizadeh A, Farhadi S, Zabardasti A (2017) Microwave-assisted rapid synthesis of graphene-analogue hexagonal boron nitride (h-BN) nanosheets and their application for the ultrafast and selective adsorption of cationic dyes from aqueous solutions. *RSC Adv* 7(85):53984–53995
69. Lin Y, Williams TV, Connell JW (2010) Soluble, exfoliated hexagonal boron nitride nanosheets. *J Phys Chem Lett* 1(1):277–283
70. Kanoun MB (2018) Tuning magnetic properties of two-dimensional MoTe_2 monolayer by doping 3d transition metals: insights from first principles calculations. *J Alloys Compd* 748:938–942

71. Kanoun MB, Goumri-Said S (2020) Tailoring optoelectronic properties of monolayer transition metal dichalcogenide through alloying. *Materialia* 12:100708
72. Muhammad R, Uqaili MA, Shuai Y, Mahar MA, Ahmed I (2018) Ab-initio investigations on the physical properties of 3d and 5d transition metal atom substituted divacancy monolayer h-BN. *Appl Surf Sci* 458:145–156
73. Gupta SK, He H, Banyai D, Si M, Pandey R, Karna SP (2014) Effect of Si doping on the electronic properties of BN monolayer. *Nanoscale* 6(10):5526–5531. <https://doi.org/10.1039/C4NR00159A>
74. Du M, Liu Q, Huang C, Qiu X (2017) One-step synthesis of magnetically recyclable Co@BN core-shell nanocatalysts for catalytic reduction of nitroarenes. *RSC Adv* 7(56):35451–35459
75. Huang C et al (2018) Dissolution and homogeneous photocatalysis of polymeric carbon nitride. *Chem Sci* 9(41):7912–7915
76. Liu D, Zhang M, Xie W, Sun L, Chen Y, Lei W (2017) Porous BN/TiO₂ hybrid nanosheets as highly efficient visible-light-driven photocatalysts. *Appl Catal B* 207:72–78
77. Lv X, Wang J, Yan Z, Jiang D, Liu J (2016) Design of 3D h-BN architecture as Ag₃VO₄ enhanced photocatalysis stabilizer and promoter. *J Mol Catal A Chem* 418–419:146–153
78. Du M (2017) One-step synthesis of magnetically recyclable Co@BN core-shell nanocatalysts for catalytic reduction of nitroarenes. *RSC Adv* 7(56):35451–35459
79. Yan J (2017) Design of 3D WO₃/h-BN nanocomposites for efficient visible-light-driven photocatalysis. *RSC Adv* 7(40):25160–25170
80. Ikram M et al (2020) Bimetallic Ag/Cu incorporated into chemically exfoliated MoS₂ nanosheets to enhance its antibacterial potential: in silico molecular docking studies. *Nanotechnology* 31(27):275704 **((in Eng))**
81. Li Y, Niu J, Zhang W, Zhang L, Shang E (2014) Influence of aqueous media on the ROS-mediated toxicity of ZnO nanoparticles toward green fluorescent protein-expressing *Escherichia coli* under UV-365 irradiation. *Langmuir* 30(10):2852–2862
82. Fang W, Chaofa X, Zheng J, Chen G, Jiang K (2015) Fabrication of Cu–Ag bimetal nanotube-based copper silicates for enhancement of antibacterial activities. *RSC Adv* 5(49):39612–39619. <https://doi.org/10.1039/C5RA06065F>
83. Espitia PJP, Soares NFF, Coimbra JSR, de Andrade NJ, Cruz RS, Medeiros EAA (2012) Zinc oxide nanoparticles: synthesis, antimicrobial activity and food packaging applications. *Food Bioprocess Technol* 5(5):1447–1464
84. Yang C, Li Q, Tang L, Xin K, Bai A, Yu Y (2015) Synthesis, photocatalytic activity, and photogenerated hydroxyl radicals of monodisperse colloidal ZnO nanospheres. *Appl Surf Sci* 357:1928–1938
85. Ahmed B et al (2020) Destruction of cell topography, morphology, membrane, inhibition of respiration, biofilm formation, and bioactive molecule production by nanoparticles of Ag, ZnO, CuO, TiO₂, and Al₂O₃ toward beneficial soil bacteria. *ACS Omega* 5(14):7861–7876
86. Lin H-F, Liao S-C, Hung S-W (2005) The dc thermal plasma synthesis of ZnO nanoparticles for visible-light photocatalyst. *J Photochem Photobiol A* 174(1):82–87
87. Du J, Gebicki JM (2004) Proteins are major initial cell targets of hydroxyl free radicals. *Int J Biochem Cell Biol* 36(11):2334–2343
88. Stephens LJ, Munuganti S, Duffin RN, Werrett MV, Andrews PC (2020) Is bismuth really the “green” metal? Exploring the antimicrobial activity and cytotoxicity of organobismuth thiolate complexes. *Inorg Chem* 59(6):3494–3508
89. Rashid M et al (2020) Photocatalytic, dye degradation, and bactericidal behavior of Cu-doped ZnO nanorods and their molecular docking analysis. *Dalton Trans* 49(24):8314–8330. <https://doi.org/10.1039/D0DT01397H>
90. Somoskovi A, Parsons LM, Salfinger M (2001) The molecular basis of resistance to isoniazid, rifampin, and pyrazinamide in *Mycobacterium tuberculosis*. *Respir Res* 2(3):164
91. Hitchings GH (1973) Mechanism of action of trimethoprim-sulfamethoxazole—I. *J Infect Dis* 128(Supplement_3):S433–S436

Publisher's Note

Springer Nature remains neutral with regard to jurisdictional claims in published maps and institutional affiliations.

Submit your manuscript to a SpringerOpen[®] journal and benefit from:

- Convenient online submission
- Rigorous peer review
- Open access: articles freely available online
- High visibility within the field
- Retaining the copyright to your article

Submit your next manuscript at ► [springeropen.com](https://www.springeropen.com)